AIAA JOURNAL
Vol. 31, No. 5, May 1993

Fluid Flow of a Row of Jets in Crossflow—A Numerical Study

S.-W. Kim* and T. J. Benson†
NASA Lewis Research Center, Cleveland, Ohio 44135

A detailed computer-visualized flowfield of a row of jets in a confined crossflow is presented. The Reynolds-averaged Navier-Stokes equations are solved by using a finite volume method that incorporates a partial differential equation for incremental pressure to obtain a divergence-free flowfield. The turbulence is described by a multiple-time-scale turbulence model. The computational domain includes the upstream region of the circular jet so that the interaction between the jet and the crossflow is simulated accurately. It is shown that the row of jets in the crossflow is characterized by a highly complex flowfield that includes a horseshoe vortex and two helical vortices whose secondary velocity components are corotating in space. It is also shown that the horseshoe vortex is a ring of reversed flows located along the circumference of the jet exit.

Nomenclature

A_j = coefficient for u_j-velocity correction
c_μ = eddy viscosity coefficient
$c_{\mu f}$ = constant coefficient, 0.09
D = diameter of circular jet
i, j = index for spatial coordinate, ($i = 1, 2, 3$ and $j = 1, 2, 3$)
k = turbulent kinetic energy, $k_p + k_t$
k_p = turbulent kinetic energy in production range
k_t = turbulent kinetic energy in dissipation range
l = turbulence length scale
P_r = production rate
p = pressure
p' = incremental pressure
U_0 = freestream velocity of crossflow
u_j = time averaged velocity, $\{u, v, w\}$
W_j = jet velocity averaged across jet cross section
x_j = Cartesian coordinates, $\{x, y, z\}$
y^+ = wall coordinate based on friction velocity
ϵ_p = energy transfer rate
ϵ_t = dissipation rate
μ = molecular viscosity
μ_t = turbulent viscosity
ρ = density

Introduction

TURBULENT flows similar to jets in crossflows can be found in a number of engineering applications, including aerospace propulsion systems. Various experimental investigations of jets in crossflows have been made to better understand turbulent flows in such engineering applications.[1-4] Numerous numerical simulations of jets in crossflows have also been made in recent years, and a compilation of various numerical investigations can be found in Claus and Vanka.[5] These numerical calculations were devoted either to the development and verification of the numerical methods to solve the three-dimensional Navier-Stokes equations or to testing the predictive capability of k-ϵ turbulence models. In either case, the calculated flowfields did not compare very well with the experimentally observed flowfield in the sense that numerical calculations failed to clearly predict the horseshoe vortex located along the circumference of the jet exit, and a detailed flow visualization has not been made yet.

In the previous calculation of a circular jet in a crossflow using a multiple-time-scale turbulence model (M-S turbulence model), the emphasis was laid on a theoretical analysis of the M-S turbulence equations to resolve the inequilibrium turbulence phenomena and to model the cascade of turbulent kinetic energy.[6] Thus, the previous investigation is largely devoted to comparing the calculated and the measured data for flowfields and concentration fields. The measured data[2] show that the turbulent transport of concentration is quite different from that of mass and momentum, in the sense that the peak concentration occurs where the tangential velocity becomes the local minimum and that the concentration field exhibits a close resemblance to the turbulence field. It can be found in Ref. 6 that the calculated velocity and concentration profiles are in very good agreement with the measured data and that the calculated velocity and concentration fields exhibit the same trend as that observed in the experiment. The calculated result also clearly exhibited the horseshoe vortex. The excellent agreement between the calculated and the measured trends indicates that the M-S turbulence model can correctly resolve the turbulent transports of mass, momentum, and concentration. It can also be found in Refs. 6-8 and the references cited therein that the numerical results for various complex turbulent flows (e.g., turbulent flows subjected to extra strains caused by streamline curvatures, interaction of multiple number of turbulence fields, and shock wave/turbulent boundary-layer interactions) obtained using the M-S turbulence model are in as good agreement with the measured data as those obtained using optimized k-ϵ turbulence models, algebraic Reynolds stress turbulence models, or Reynolds stress turbulence models for each flow case. The capability of the M-S turbulence equations to solve widely different complex turbulent flows is attributed to their capabilities to resolve the inequilibrium turbulence phenomena and to model the cascade of turbulent kinetic energy. These capabilities are discussed subsequently, whereas details of the M-S turbulence model can be found in Refs. 6-8.

In complex turbulent flows, the production and dissipation rates of the turbulent kinetic energy vary widely in space so that the shape and the frequency domain of the spectral density also vary widely in space. Such a state of turbulence is called "inequilibrium turbulence."[6-8] The influence of inequilibrium turbulence on turbulent transport of mass and momentum can be observed in the eddy viscosity coefficient reduced from measured data.[9-11] The reduced data show that the eddy viscosity coefficient is decreased as P_r/ϵ_t is increased, and it is increased as P_r/ϵ_t is decreased. Thus, the develop-

Presented as Paper 92-0534 at the AIAA 30th Aerospace Sciences Meeting, Reno, NV, Jan. 6-9, 1992; received Jan. 17, 1992; revision received Sept. 8, 1992; accepted for publication Sept. 16, 1992.

*Resident Research Associate, Internal Fluid Mechanics Division, MS 5-11. Member AIAA.
†Research Engineer, Internal Fluid Mechanics Division, MS 5-11.

ments of the mean fluid flow and the turbulence field are influenced by the spatially varying turbulent viscosity, and the spatially varying turbulent viscosity depends not only on the turbulence intensity but also on the level of inequilibrium turbulence. The capability to resolve the inequilibrium turbulence phenomenon originates from describing the turbulence length scale and the turbulent viscosity using the energy transfer rate, i.e., $l = c_{\mu f}k^{3/2}/\epsilon_p$ and $\mu_t = \rho\sqrt{k}l = \rho c_{\mu f}k^2/\epsilon_p$. Rewriting the turbulent viscosity in a form compatible with that of k-ϵ turbulence models yields $\mu_t = \rho c_\mu k^2/\epsilon_t$ where $c_\mu = c_{\mu f}\epsilon_t/\epsilon_p$ is the eddy viscosity coefficient. Thus, the influence of inequilibrium turbulence on turbulence transport is described as a function of ϵ_t/ϵ_p, and ϵ_t/ϵ_p is a function of P_r/ϵ_t (Refs. 6–8). In k-ϵ turbulence models, the turbulence length scale and the turbulent viscosity are defined using the dissipation rate, i.e., $l = c_{\mu f}k^{3/2}/\epsilon_t$ and $\mu_t = \rho\sqrt{k}l = \rho c_{\mu f}k^2/\epsilon_t$. Because of the use of a constant eddy viscosity coefficient, the turbulent viscosity in a strongly turbulent region ($P_r/\epsilon_t > 1$) is overpredicted and that in a weakly turbulent region ($P_r \approx 0$) is underpredicted. As an example, the underpredicted reattachment locations for a flow over a backward-facing step obtained using k-ϵ turbulence models are caused by the overpredicted turbulent viscosity along the reattaching shear layer.[7]

In turbulent flows, the energy-containing large eddies are generated by the instability of the mean fluid flow, the large eddies cascade to finer eddies, and the fine-scale eddies are dissipated by the viscous forces. The energy-containing large eddies are characterized by low frequencies and large values of k_p/k_t, and the fine-scale eddies are characterized by higher frequencies and small values of k_p/k_t.[6] The ratio of k_p/k_t is determined by the shape and the frequency domain of each spectral density (see Ref. 6 for further details). In the M-S turbulence equations, the capability to model the cascade process is achieved by solving the convection-diffusion equations for k_p and k_t separately. For highly complex turbulent flows, large eddies generated in the upstream region are convected in the downstream direction. In such a downstream region, the ratios of P_r/ϵ_t and ϵ_t/ϵ_p are influenced by the convected eddies (i.e., the large value of k_p/k_t). Thus, the inequilibrium turbulence is also influenced by the cascade of turbulent kinetic energy.

The near-wall turbulence is described by a "partially low Reynolds number" near-wall turbulence model.[12] In the model, only the turbulent kinetic energy equations are extended to include the near-wall low turbulence region, and the energy transfer rate and the dissipation rate inside the near-wall layer are obtained from algebraic equations. It can be found in Refs. 6–8 that the partially low Reynolds number near-wall turbulence model (when used together with the M-S turbulence model) yields highly improved numerical results compared with those obtained using wall functions. Successful prediction of the horseshoe vortex in this study as well as in the previous numerical calculation of a circular jet in a crossflow[6] is also attributed to the use of the partially low Reynolds number near-wall turbulence model.

The numerical method is a finite volume method based on a pressure correction algorithm.[13–15] In this method, all flow variables except pressure are located at the same grid points, whereas pressure is located at the centroid of a cell formed by the neighboring velocity grid points. The pressure for a divergence-free velocity field is obtained by solving a partial differential equation for incremental pressure. Derivation of the incremental pressure equation and calculations of a three-dimensional lid-driven cavity flow and a laminar flow through a 90 deg-bend square duct can be found in Ref. 13. It is shown in that reference that the numerical results for the cavity flow obtained using the present numerical method compare more favorably with the measured data than those obtained using a formally third-order-accurate quadratic upwind interpolation scheme. It is also shown in Ref. 13 that the present method yields a grid independent solution for the curved duct flow with as small as $68 \times 18 \times 33$ grid points and that the calculated results are in excellent agreement with the measured data. Calculations of unsteady flows over a circular cylinder and a square cylinder also show that the present numerical method yields significantly improved numerical results compared with those obtained using a formally third-order-accurate quadratic upwind interpolation scheme.[15] These observations indicate that strongly enforcing the conservation of mass is as important as or more important than employing a higher order differencing scheme for incompressible flows.

Numerical Method

The incompressible turbulent flow equations are given as

$$\frac{\partial}{\partial x_j}(\rho u_j) = 0 \tag{1}$$

$$\frac{\partial}{\partial x_j}(\rho u_i u_j) - \frac{\partial}{\partial x_j}\left\{(\mu + \mu_t)\left(\frac{\partial u_i}{\partial x_j} + \frac{\partial u_j}{\partial x_i}\right)\right\} = -\frac{\partial}{\partial x_i}\left(p + \frac{2}{3}\rho k\right) \tag{2}$$

where repeated indices imply summation over the index unless otherwise stated. The momentum equation and the turbulence equations are solved by a finite volume method using the power-law upwind differencing scheme.[16] The conservation of mass equation is replaced by a partial differential equation for incremental pressure and is given as

$$\frac{\partial}{\partial x_j}\left(\frac{1}{A_j}\frac{\partial p'}{\partial x_j}\right) = -\frac{\partial}{\partial x_j}(\rho u_j^*) \tag{3}$$

where u_j^* denotes the velocity obtained by solving the momentum equations, and it may not satisfy the conservation of mass until the solutions are fully converged.[13,14] The last term in Eq. (3) represents the mass imbalance.

As a central differenced finite volume equation for self-adjoint second-order elliptic partial differential equations is strongly diagonally dominant, the discrete pressure correction equation obtained by applying the standard finite volume method to Eq. (3) is strongly diagonally dominant even for highly skewed and graded meshes. Also, the present pressure correction method yields a unique solution since the incremental pressure is driven only by the mass imbalance as shown in Eq. (3). For clarity, the differences between the present pressure correction algorithm and various other algorithms are explained subsequently.

In various pressure correction algorithms,[14–16] the discrete pressure correction equation is obtained by inserting a discrete velocity-pressure gradient relationship obtained from the momentum equation into the conservation of mass equation. The use of these pressure correction algorithms for the pressure-staggered mesh yields a system of discrete pressure correction equations that lacks diagonal dominance. In such a case, the mass imbalance at a pressure grid point produces large corrections for pressures at adjacent pressure grid points, and velocity-pressure decoupling occurs.[14] Enhancing the diagonal dominance of such discrete pressure correction equations by incorporating a very small under-relaxation parameter lets velocity-pressure decoupling occur very slowly, but it cannot prevent velocity-pressure decoupling.

The difference between the present pressure correction method and various other methods becomes the most distinctive in the case of a pressure-staggered, orthogonal mesh aligned with Cartesian coordinates; that is, the present method yields a strongly diagonally dominant seven-diagonal system of equations for the incremental pressure, whereas various other methods yield a 27-diagonal system of equations that lacks diagonal dominance. As can be found in the following Numerical Results section, a highly skewed and graded mesh needs to be used at and near the jet exit. Inclusion of the upstream region of the jet in the present numerical simulation is made possible due to the strongly convergent nature of the numerical method to solve the Reynolds-averaged Navier-Stokes equations.

Numerical Results

The row of equally spaced circular jets in a confined crossflow[1] is schematically shown in Fig. 1. The distance from the center of a circular jet to that of an adjacent jet is four times the diameter of the circular pipe, and the diameter of each circular pipe is 0.0254 m. The channel height is four times the diameter of the circular pipe. The inlet velocity of the crossflow is 10.8 m/s, and the ratio of $W_j/U_0 = 2.3$.

The computational domain is shown in Fig. 2, where $(x, y, z) = (0, 0, 0)$ refers to the center of a jet at the jet exit. The inlet boundary is located at $x/D = -3.2$. The inlet boundary conditions for the crossflow are obtained from measured data for a fully developed boundary-layer flow over a flat plate.[17] The nondimensionalized measured data are scaled to yield a boundary-layer thickness of 0.005 m at the inlet boundary. The exit boundary is located at $x/D = 13.7$, and a vanishing gradient boundary condition is used for all flow variables. As in the previous calculations of the jets in crossflow compiled in Ref. 5, the computational domain in y direction extends from $y/D = 0$ plane to $y/D = 2$ plane, and symmetry boundary conditions are prescribed on these planes. Both the measured data[4] and the previous numerical results[6] show that the jet and the crossflow interact strongly with each other at the jet exit so that the influence is propagated toward the upstream direction of the jet. Consequently, the vertical velocity and the total pressure vary widely across the jet exit.

Therefore, neither the constant vertical velocity nor the constant total pressure boundary condition used in a number of previous numerical calculations[5] is a truly valid approximation for the fluid flow at the jet exit. The extent that the influence can propagate depends on the ratio of W_j/U_0. For such a high value of $W_j/U_0 = 2.3$, the influence of the interaction between the jet and the crossflow becomes weak for $z/D < -0.4$, and, hence, the upstream boundary of the jet is located at $z/D = -0.4$ plane. The inlet boundary conditions for the jet are obtained from measured data for a fully developed pipe flow.[18] The nondimensionalized measured data are scaled to yield a bulk velocity of 24.8 m/s at the jet inlet

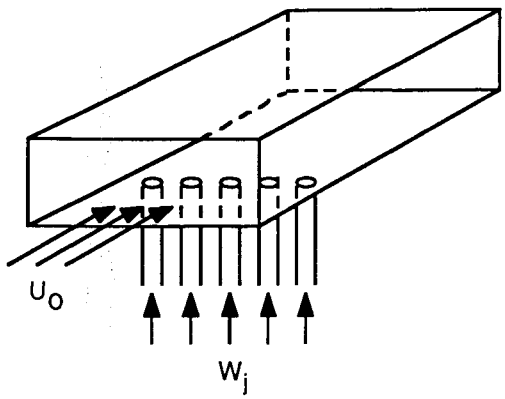

Fig. 1 Nomenclature for a row of circular jets in confined crossflow.

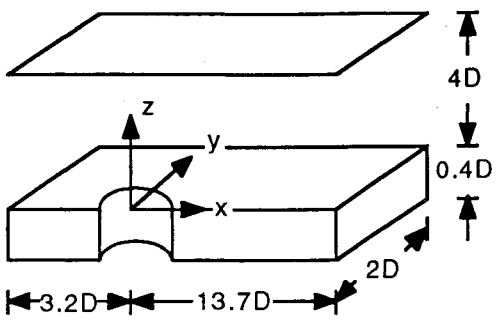

Fig. 2 Computational domain.

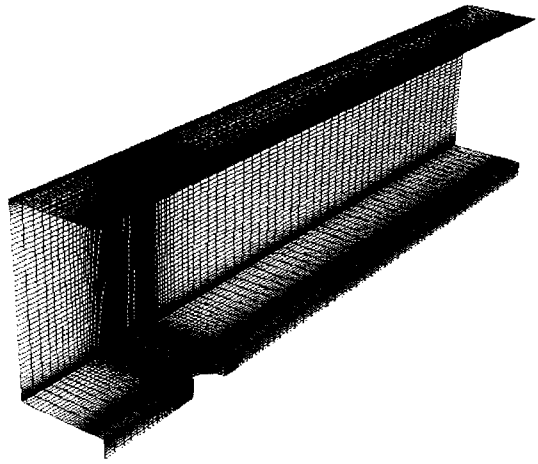

a) Entire domain

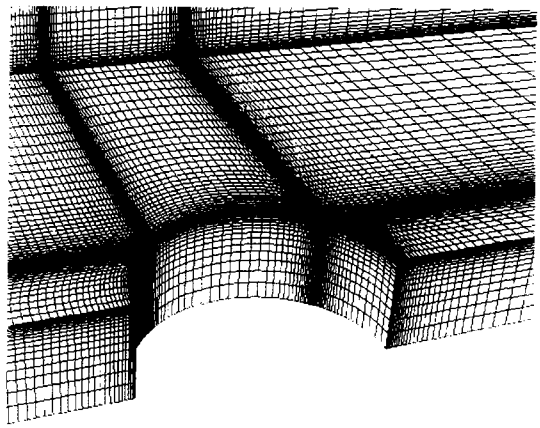

b) Vicinity of jet exit

Fig. 3 Discretization of computational domain.

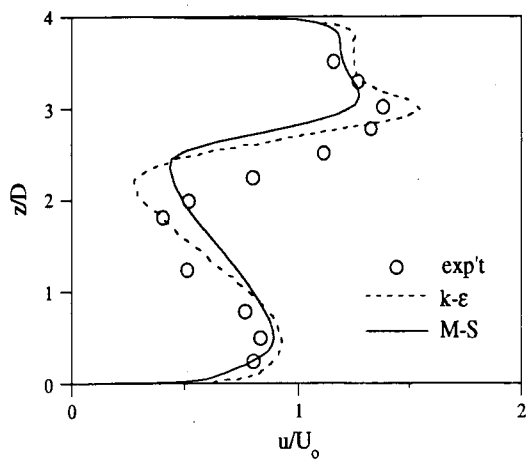

Fig. 4 Velocity profiles at $x/D = 4$.

boundary. The no-slip boundary condition for velocities and vanishing turbulent kinetic energy are prescribed at the solid wall boundary.

The computational domain is discretized by $165 \times 59 \times 83$ grid points in x-, y-, and z-coordinate directions, respectively. The mesh for the entire flow domain and that near the jet exit are shown in Fig. 3. The smallest mesh size in the direction normal to the wall is 0.9×10^{-4} m ($y^+ \approx 2.0$ based on the fully developed pipe flow entering the circular pipe), and the largest mesh size near the exit of the duct is approximately 0.31 times the jet diameter. The grid size in the normal direction to the wall is increased by a factor of approximately 1.1.

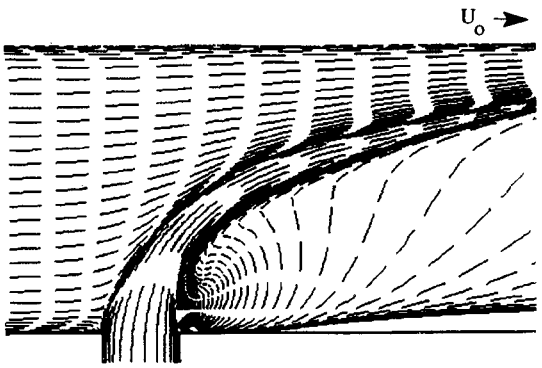

a) Discrete particle trajectories on $y/D = 0$ plane

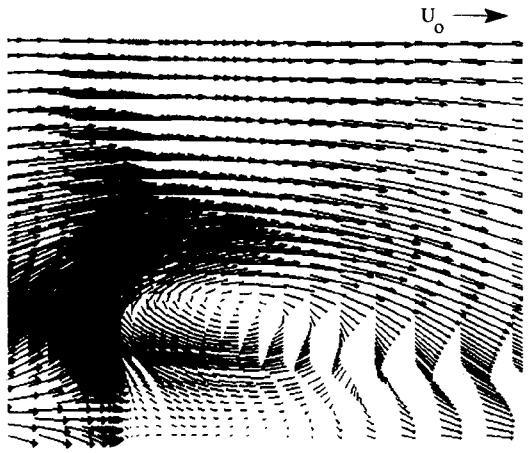

b) Velocity vectors on $z/D = 0.47$ plane

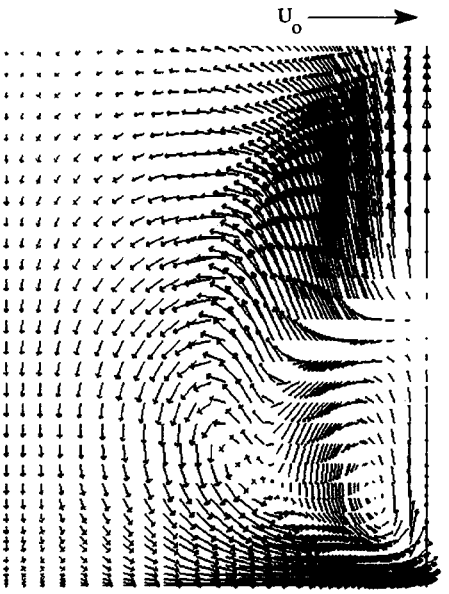

c) Velocity vectors on $x/D = 0.93$ plane

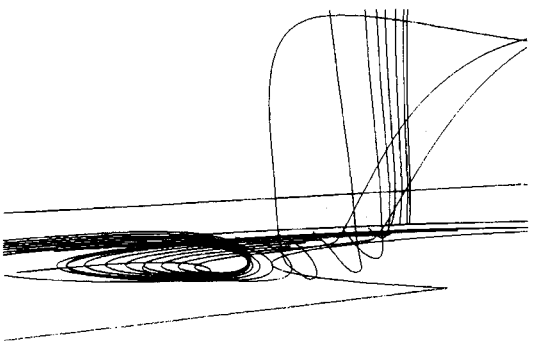

d) Particles trajectories along the horseshoe vortex

Fig. 5 Fluid flow of jets in crossflow.

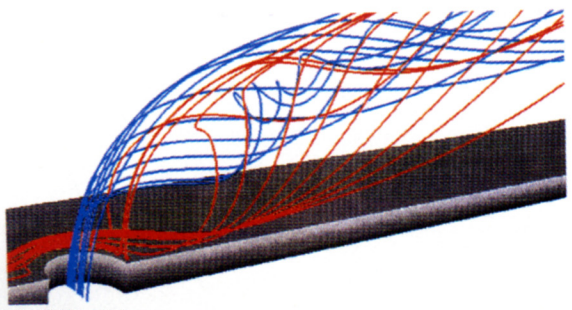

a) Side view

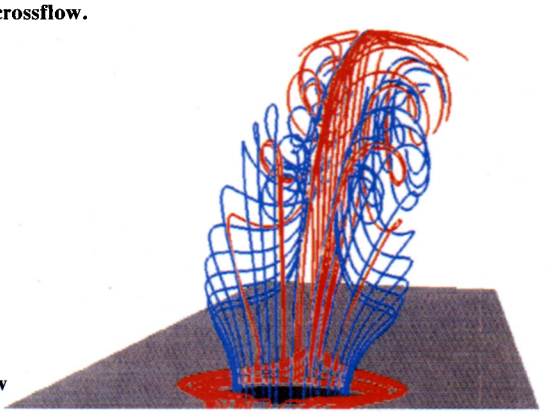

b) Front view

Fig. 6 Particle trajectories for jets in crossflow.

Thus, the mesh near the jet exit is fine enough to resolve the details of the interaction between the fluid streams and to capture the horseshoe vortex located around the circumference of the jet exit. The partition between the near-wall layer and the external region is located at $y^+ \approx 100$ (based on the fully developed flat plate flow at the inlet of the duct), and 10 grid points are allocated inside the near-wall layer. It can be found in Refs. 6–8 that approximately 10 grid points inside the near-wall layer are sufficient to resolve details of the near-wall fluid flow and turbulence structures for various separated and recirculating flows, including shock-separated boundary-layer flows.

The error norm used for the convergence test is given as

$$|e|_l = \max\left\{\text{abs}\left[\frac{A_l^k - A_l^{k-1}}{A_{l,0}^k}\right]_{j=1,N}\right\} \leq \epsilon_l$$

where A_l^k is the lth flow variable at the kth iteration, $A_{l,0}^k$ the maximum lth flow variable at the kth iteration, N the total number of grid points, and ϵ_l the convergence criterion for each flow variable. For $\epsilon_l = 1.0 \times 10^{-5}$, the converged solutions are obtained in approximately 1000 iterations, and the relative imbalance of the mass flow rate leaving the flow domain with respect to that entering the flow domain is less than 1.5×10^{-4}.

The calculated tangential velocity profile at $x/D = 4$ is shown in Fig. 4. It can be seen in the figure that the velocity profiles obtained using the k-ϵ and the M-S turbulence equations exhibit the same level of agreement with the measured data. However, the present numerical calculation using the M-S turbulence equations successfully predicts the detailed flow structure, such as the horseshoe vortex, whereas the k-ϵ turbulence models cannot.[5] Recall that the fluid flow in the

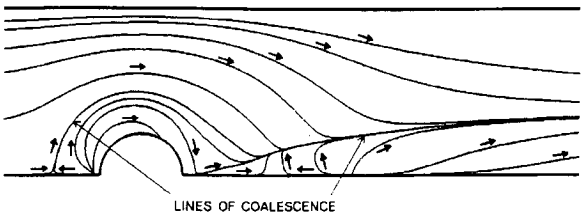

Fig. 7 Oil flow simulation for bottom wall.

downstream region of the jets approaches a developing duct flow as shown in Fig. 1, and, hence, the symmetry boundary condition used at $y/D = 2$ cannot accurately represent the actual fluid flow. Thus, the discrepancy between the measured and the calculated axial velocity profiles is caused mostly by the symmetry boundary condition applied at $y/D = 2$ plane.

Discrete particle trajectories on the symmetry plane ($y/D = 0$) are shown in Fig. 5a. A continuous particle trajectory can best describe the time history of a particle path, whereas it cannot describe the magnitude of the velocity. On the other hand, a velocity vector plot can best describe the direction and the magnitude of the velocity, whereas it cannot describe the time history of a particle path. In this regard, the discrete particle trajectories can best describe the particle path and the magnitude of the velocity. It can be seen in the figure that the interaction between the jet and the top wall ($z/D = 4$ plane) creates a defective velocity profile near the top wall. It can be seen in Fig. 4 that the present numerical result and that obtained using a k-ϵ turbulence model exhibit the velocity defect near $z/D = 4$, whereas the measured velocity profile does not show any velocity defect. This discrepancy is partly caused by the uncertainty in the measurement and partly by the symmetry boundary condition applied at $y/D = 2$ plane. The primary vortex located behind the jet is shown in Fig. 5b. The primary vortex is generated by the jet that acts as an internal blockage for the crossflow. The two-dimensional velocity vectors of the primary vortex are similar to those found in flows over circular cylinders. However, the primary vortex is a three-dimensional helical vortex, and, hence, it is quite different from those of flows over circular cylinders.

The velocity vectors for the primary vortex and the secondary vortex at $x/D = 0.93$ plane are shown in Fig. 5c. The secondary vortex is generated by the shearing force exerted by the jet. Particle trajectories viewed along the axis of the horseshoe vortex are shown in Fig. 5d. For jets in crossflows, the crossflow is decelerated by the jet, and a strong adverse pressure gradient is formed in the forward region of the jet. The fluid particles in the region very close to the wall carry only a negligible amount of momentum. These particles are reversed by the strong adverse pressure gradient, and the reversed flow in the forward region of the jet forms the horseshoe vortex.

It can be found in Ref. 3 that the horseshoe vortex is formed around the jet for W_j/U_0 greater than 0.6. At a large crossflow velocity, the axial velocity is by far larger than the other velocity components; hence the particles do not exhibit an extensive rotatory motion. It can also be found in the experiment of fluid flow around a surface mounted cylinder[19] that the horseshoe vortex exhibits a fully developed rotatory motion only at a very small crossflow velocity that is a few times smaller than the present case. It can also be found in Ref. 19 that the flow structure of the horseshoe vortex can be observed most clearly by the velocity vectors inside the horseshoe vortex. The calculated velocity vectors inside the horseshoe vortex for the jets in crossflow are shown later in this section.

A side view and a front view of the three-dimensional particle trajectories are shown in Figs. 6a and 6b, respectively. It can be seen in Fig. 6a that the fluid particles near the jet edge carry less momentum, and, hence these particles are quickly entrained to the helical vortices in the wake region of the jet. The particle trajectories show that the large eddy mixing occurs in the wide region of the jet edge and that the fluid particles in the center region of the jet do not mix easily with the crossflow. The helical nature of the primary vortex can be most easily observed in the front view of the particle trajectories (see Fig. 6b). It is also shown in Fig. 6b that the jet is split into two symmetric parts by the reversed flow of the primary vortex.

A simulated oil flow on the bottom wall is shown in Fig. 7. The surface streaklines are obtained by tracking the particle trajectories confined on $z/D = 0.004$ plane, which is one grid point away from the wall. The line of coalescence in the forward region of the jet is caused by the horseshoe vortex located along the circumference of the jet exit, and that in the wake region is mostly caused by the viscous force exerted by the external fluid flow.

The horseshoe vortex located along the circumference of the jet exit is shown in Fig. 8. The velocity vectors shown in the

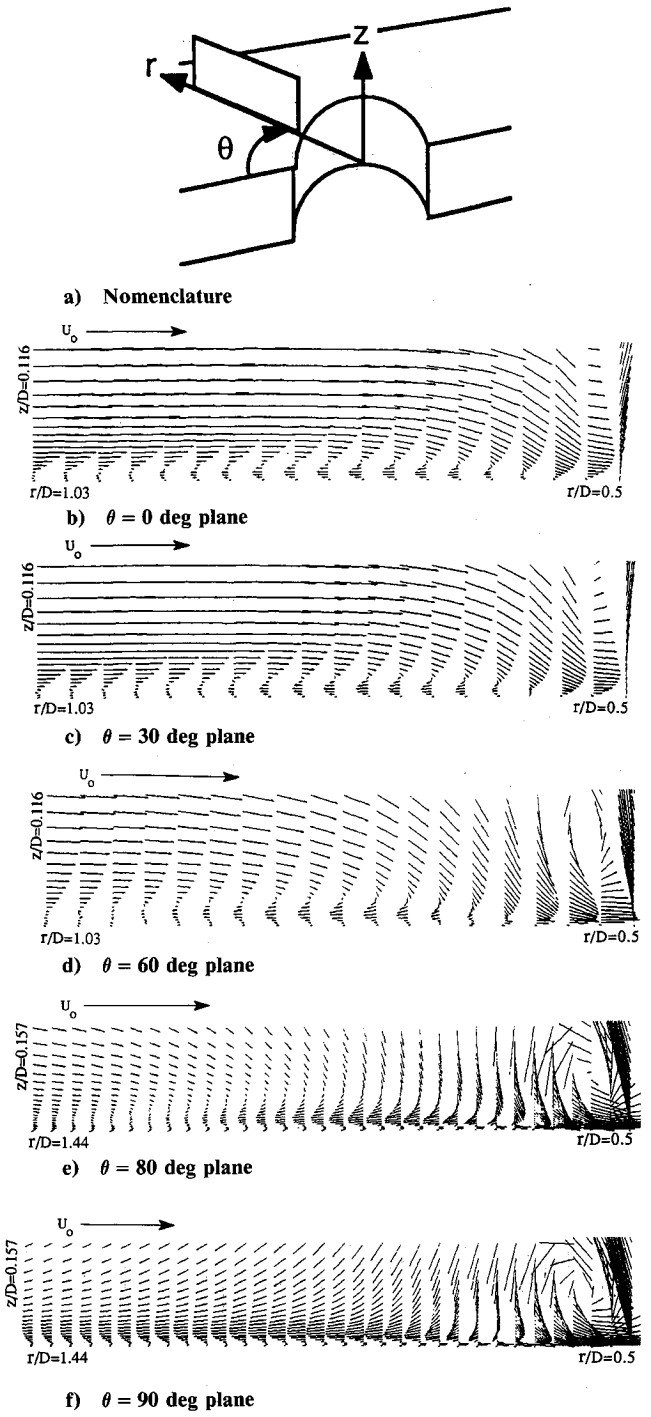

Fig. 8 Horseshoe vortex located along the circumference of the jet exit.

figure are obtained by projecting the three-dimensional velocity vectors onto the (r, z) plane shown in Fig. 8a. As the fluid particles turn around the jet, the strength of the vorticity is increased, and, thus, the size of the horseshoe vortex is also increased (see Fig. 8d). It can also be seen in Fig. 8d that the secondary vortex began to form at $r/D = 0.5$ by the shearing action of the jet. For $\theta > 80$ deg, the horseshoe vortex began to be dissipated by the stronger counter-rotating secondary vortex (see Figs. 8e, 8f). As the fluid particles travel farther in the downstream direction, the horseshoe vortex is mostly smeared out by the stronger secondary vortex. As can be seen in Figs. 8b–8d, the horseshoe vortex is a ring of reversed flow.

Conclusions and Discussion

The fluid flow of a row of jets in a confined crossflow is characterized by a highly complex flowfield that includes a primary vortex located in the wake region of the jet, a secondary vortex located in the side region of the jet, and a horseshoe vortex located along the circumference of the jet exit. The primary vortex is formed by the jet that acts as an internal blockage for the crossflow. In this regard, the fluid flow behind the jet is similar to that found in two-dimensional flows over circular cylinders. However, the nature of the primary vortex is quite different from that of flows over circular cylinders since the primary vortex is essentially a helical vortex. At downstream locations, the jet is split into two symmetric parts by the reversed flow of the primary vortex. The secondary vortex is generated by the shearing force exerted by the jet. The primary and the secondary vortices are both helical vortices, and their secondary velocity components are corotating in space. The horseshoe vortex is a ring of reversed flow and is generated by the strong adverse pressure gradient formed by the jet in crossflow.

The successful prediction of the horseshoe vortex and the flowfield inside the horseshoe vortex is attributed to the numerical method that yields accurate numerical results for highly graded and skewed meshes and to the M-S turbulence model that can resolve the complex turbulence field. The M-S turbulence model can resolve the influence of the inequilibrium turbulence and can model the cascade of the turbulent kinetic energy, and these capabilities are not found in various single time-scale turbulence models. In this study, the upstream region of the circular jet is included into the computational domain so that the interaction between the jet and the crossflow is simulated accurately. Consider that the upstream region of the jet was excluded from the computational domain, and either a constant vertical velocity or a constant total pressure was prescribed at the jet exit in various numerical simulations of the jets in crossflow compiled in Ref. 5. The constant vertical velocity or the constant total pressure boundary condition overestimates the rigidity (or, equivalently, underestimates the compliance) of the jet compared to the actual fluid flow, so that the experimentally observed horseshoe vortex located along the circumference of the jet exit[3] could have been predicted more easily in these numerical calculations than in the present calculation. However, Claus and Vanka[5] showed that the k-ϵ turbulence model fails to predict the horseshoe vortex even with the use of a highly fine $256 \times 96 \times 96$ mesh. The failure to predict the horseshoe vortex is attributed partly to the numerical method, which cannot yield accurate numerical results for the highly complex fluid flow, and partly to the inability of the k-ϵ turbulence models, which cannot resolve the complex turbulence field.

Acknowledgment

The authors would like to express their sincere thanks to J. D. Holdeman for many valuable discussions.

References

[1]Khan, Z. A., "Opposed Jets in Crossflow," Ph.D. Dissertation, Mechanical Engineering Dept., Imperial College of Science and Technology, London, 1982.

[2]Crabb, D., Durao, D. F. G., and Whitelaw, J. H., "A Round Jet Normal to a Crossflow," *Journal of Fluid Engineering,* Vol. 103, March 1981, pp. 142–152.

[3]Foss, J., "Interaction Region Phenomena for the Jet in a Crossflow Problem," Univ. of Karlsruhe, Rept. SFB 80/E/161, Karlsruhe, Germany, 1980.

[4]Andreopoulos, J., "Measurements in a Jet-Pipe Flow Issuing Perpendicularly into a Cross Stream," *Journal of Fluid Engineering,* Vol. 104, Dec. 1982, pp. 493–499.

[5]Claus, R. W., and Vanka, S. P., "Multigrid Calculations of a Jet in Cross Flow," AIAA Paper 90-0444, AIAA 28th Aerospace Sciences Meeting, Reno, NV, Jan. 1990.

[6]Kim, S.-W., and Benson, T. J., "Calculation of a Circular Jet in Crossflow with a Multiple-Time-Scale Turbulence Model," *International Journal of Heat and Mass Transfer,* Vol. 35, No. 10, 1992, pp. 2357–2365.

[7]Kim, S.-W., "Calculation of Reattaching Shear Layers in Divergent Channel with a Multiple-Time-Scale Turbulence Model," *AIAA Journal,* Vol. 29, No. 4, 1991, pp. 547–554.

[8]Kim, S.-W., "Numerical Investigation of Separated Transonic Turbulent Flows with a Multiple-Time-Scale Turbulence Model," *Numerical Heat Transfer,* Pt. A, Vol. 18, 1990, pp. 149–171.

[9]Rodi, W., "The Prediction of Free Boundary Layers by Use of a Two-Equation Model of Turbulence," Ph.D. Dissertation, Univ. of London, London, 1972.

[10]Launder, B. E., "A Generalized Algebraic Stress Transport Hypothesis," *AIAA Journal,* Vol. 20, No. 3, 1982, pp. 436–437.

[11]Kim, S.-W., and Chen, Y.-S., "A Finite Element Calculation of Turbulent Boundary Layer Flows with an Algebraic Stress Turbulence Model," *Computer Methods in Applied Mechanics and Engineering,* Vol. 66, No. 1, Jan. 1988, pp. 45–63.

[12]Kim, S.-W., "A Near-Wall Turbulence Model and Its Application to Fully Developed Turbulent Channel and Pipe Flows," *Numerical Heat Transfer,* Pt. B, Vol. 17, 1990, pp. 101–122.

[13]Kim, S.-W., "Calculations of Separated 3-D Flows with a Pressure-Staggered Navier-Stokes Equations Solver," NASA CR-187065, 1991.

[14]Kim, S.-W., "On the Anomaly of Velocity-Pressure Decoupling in Collocated Mesh Solutions," NASA TM-103769, 1991.

[15]Kim, S.-W., and Benson, T. J., "Comparison of the SMAC, PISO and Iterative Time-Advancing Schemes for Unsteady Flows," *Computers and Fluids,* Vol. 21, No. 3, 1992, pp. 435–454.

[16]Patankar, S. V., *Numerical Heat Transfer and Fluid Flow,* McGraw-Hill, New York, 1980.

[17]Klebanoff, P. S., "Characteristics of Turbulence in a Boundary Layer with Zero Pressure Gradient," NACA Rept. 1247, 1955.

[18]Laufer, J., "The Structure of Turbulence in Fully Developed Pipe Flow," NACA TR-1174, 1954.

[19]Eckerle, W. A., and Awad, J. K., "Effect of Freestream Velocity on the Three-Dimensional Separated Flow Region in Front of a Cylinder," *Journal of Fluid Engineering,* Vol. 113, March 1991, pp. 37–44.